Powder aerosol deposited calcium cobaltite as textured P-type thermoelectric material with power factors approaching single crystal values

Daniel Paulus [a],[*], Sophie Bresch [b], Ralf Moos [a], Daniela Schönauer-Kamin [a]

[a] *Department of Functional Materials, University of Bayreuth, Bayreuth 95440, Germany*
[b] *Advanced Multimaterial Processing, Bundesanstalt für Materialforschung und –prüfung, Berlin, Germany*

ARTICLE INFO

ABSTRACT

In this work, the thermoelectric material calcium cobaltite Ca₃Co₄O₉ (CCO), a promising p-type conducting thermoelectric oxide with anisotropic properties, was processed by the powder aerosol deposition method (PAD) to form a dense ceramic CCO film with a thickness in the μm range. The prepared films were characterized regarding their microstructure and thermoelectric properties between room temperature and 900 °C. After heat treatment at 900 °C, the CCO PAD film in-plane shows excellent properties in terms of electrical conductivity (280 S/cm at 900 °C) and Seebeck coefficient (220 μV/K at 900 °C). The calculated power factor in-plane (*ab*) reaches with 1125 μW/(m K^2) 40 % of the single crystal value, surpassing the known-properties of CCO bulk ceramics. Examination of the microstructure shows a strong fiber texture of the film as well as a strong coarsening of the grains during the first heat treatment up to 900 °C.

1. Introduction

Thermoelectric generators convert a temperature difference directly into electricity by utilizing the Seebeck effect. Typically, a thermoelectric generator consists of thermocouples connected electrically in series and thermally in parallel [1,2]. In most cases, each thermocouple is made of a p-type material with a positive Seebeck coefficient and an n-type material with a negative Seebeck coefficient [1,3]. The Seebeck coefficient S describes the induced voltage per Kelvin in the material. For a high electrical power output of the generator, thermoelectric materials should have high absolute Seebeck coefficients as well as a high electrical conductivity σ. This is summarized in the power factor $PF = S^2 \bullet \sigma$. A measure for the efficiency of thermoelectric generators is the figure of merit $ZT = (PF \bullet T) / \kappa$, with the thermal conductivity κ of the thermoelectric material and with absolute temperature T [4,5]. Since the efficiency of thermoelectric generators is significantly lower than that of competing energy conversion processes, their use in the field of heat recovery is limited [6,7]. Thermoelectric generators, instead, have a high potential in the field of energy harvesting where a quasi-unlimited source of waste heat can be exploited to provide electrical power in the range of μW to mW, for e.g., self-powered sensor systems. Thermoelectric materials for energy harvesting should

therefore be optimized primarily for high power factors (and only secondarily for low thermal conductivity) [8].

Around room temperature, doped bismuth telluride is used commercially with PF = 6 mW/mK^2 [9]. However, bismuth telluride is only stable up to 250 °C in air [10]. For high-temperature applications in the range of up to 800 °C, thermoelectric oxides form a promising class of materials [11,12]. They are stable at high-temperatures, oxidation resistant, and less toxic than non-oxide materials. The most promising p-type oxide material is calcium cobaltite Ca₃Co₄O₉ (CCO or Co349). It has a misfit-layered crystal structure [13] consisting of two sublattices: Ca₂CoO₃ of the triple rock salt type and the hexagonal CoO₂. Lattice misfits occur between the two sublattices. Due to the layered crystal structure, the physical and thermoelectric properties of the single crystal are strongly anisotropic. The electrical conductivity of Ca₃Co₄O₉ single crystal whiskers is about 500–1000 times higher in the *ab*-direction (parallel to the layers) than in the *c*-direction (normal to the layers). The power factor PF_{ab} of single crystals reaches up to 3 mW/mK^2 at 600 °C [10,14]. For polycrystalline highly textured specimens (hot-pressed with 10 MPa [15]), the Seebeck coefficient in the *ab*-direction is 1.06 times higher than in the *c*-direction, and the thermal conductivity in the *ab*-direction is two times higher than in the *c*-direction. Due to the increased grain growth in the *ab*-direction, undoped calcium cobaltite

has a platelet- to lenticular-shaped particle morphology [10].

$Ca_3Co_4O_9$ decomposes at 926 °C into $Ca_3Co_2O_6$ and CoO [16], limiting its sintering temperature to below 926 °C. Conventionally sintered $Ca_3Co_4O_9$ has a high porosity (40 %) and only a low degree of texture (multiple of random distribution MRD = 3.5) [17]. This leads to an inferior power factor PF_{ab} in the range of 75 $\mu W/mK^2$ [17,18], which is only 2 % of the single crystal. To increase the thermoelectric performance (especially the power factor) of polycrystalline $Ca_3Co_4O_9$, an increase of the sinter density and/or a texture is desirable. The textured polycrystalline material should later be used in *ab*-direction. Tape-casting combined with pressure assisted sintering (PAS) increases the texture (MRD = 9.3) [19], leading to PF_{ab} = 120 $\mu W/mK^2$ [20]. Hot pressing with 30 MPa increases both sinter density (96 %) and the texture (MRD = 22). The samples exhibited PF_{ab} = 600 $\mu W/mK^2$, which is already 20 % of the single crystal value [17]. Power factor, sinter density, and degree of texture increase with increasing pressure level during hot pressing [17,19].

These results show that for optimized thermoelectric properties of CCO, a high density of the material with low porosity is necessary, combined with a high degree of texturing in the preferred *ab*-direction.

To manufacture dense ceramic films or materials, the use of the powder aerosol deposition method (PAD) has been increasingly investigated in recent years. PAD is a method to obtain dense ceramic films in the thickness range of 0.5 μm to 100 μm directly at room temperature from the synthesized starting powders without any subsequent high-temperature step. In literature, especially in the early and fundamental studies, it is often referred to as aerosol deposition method (ADM) [21,22]. Its applicability has been shown for various materials and thermoelectric materials, too [23–28]. The ceramic powder particles of appropriate size are accelerated in the PAD process. The impact of the particles with suitable kinetic energy on the substrate leads to the formation of dense ceramic films at room temperature. The resulting films are typically characterized by a high density with small grains and (almost) no pores. A nanocrystalline microstructure is obtained [21]. Due to the room temperature impact consolidation (RTIC) mechanism and the densification of the films by the hammering effect, the crystal lattice of the nanometer-sized particles is deformed [22,26]. This results in a microstrain in the crystal lattice, which goes along with a reduced charge carrier mobility. A subsequent moderate thermal annealing can relax the microstrain in the crystal lattice. A reduction of the microstrain in the PAD film follows and increases the charge carrier mobility and improves therefore the electrical properties, e.g., it increases the electrical conductivity of the film [29–33]. The nanostructured morphology can also affect the thermal lattice conductivity by hindering the phonon migration [24]. A decrease in the thermal conductivity follows, that can be beneficial for a higher ZT value of thermoelectric materials. Additionally, PAD films are very flexible and therefore the preparation of planar flexible TEGs is possible, as has already been shown for Bi_2Te_3 PAD films [28]. The known properties of films produced by the PAD process could therefore have a positive effect on the thermoelectric properties of CCO. A first successful application of the PAD process for CCO was presented by Yoon et al. [34] and Nakamura et al. [35]. Both studies showed a fiber texture of the aerosol deposited films with comparable values of the Seebeck coefficient and electrical conductivity. Additionally, effects of sintering the PAD films at high temperatures on the thermoelectric properties are discussed and thermoelectric properties comparable to bulk materials have been reached after thermal annealing at 900 °C.

Since multi-layered thick-film type thermoelectric generators and transversal thermoelectric generators are still of interest for energy harvesting [36–43], our work focuses on the enhancement of the thermoelectric properties of textured CCO films prepared by powder aerosol deposition. Additionally, the question if a powder with a 2D-symmetric crystal structure can be used to produce dense and textured PAD films, also without thermal annealing, will be answered. At the end, it will be shown that these PAD CCO films reach the highest PF for polycrystalline CCO materials (only single crystals exhibit higher values).

2. Materials and methods

For this study, as-synthesized calcium cobaltite powder was used, and thick films were processed by the powder aerosol deposition method (PAD). The calcium cobaltite $Ca_3Co_4O_9$ (CCO) powder was synthesized as described in [44] by a mixed-oxide route. Stoichiometric amounts of $CaCO_3$ (99 %, low-alkali, Riedel-de Haën, Seelze, Germany) and Co_3O_4 (99.97 %, ChemPUR, Karlsruhe, Germany) were mixed by attrition milling (moliNEx, Netzsch) with ZrO_2 grinding media for 45 min (d_{50} = 1.5 μm). After calcination for 12 h at 900 °C in air, the calcined CCO powder was crushed in a planetary ball mill (using grinding jars and grinding media) for 20 min and finally attrition milled for 15 min.

In the next step, CCO films on alumina substrates were prepared by powder aerosol deposition. Therefore, the CCO powders were sieved and dried at 200 °C in a drying oven. Some grams of the powders were filled in a fluidized bed aerosol generation chamber, which is located on a vibrating table (For details about the device please check SI). By a continuous carrier gas flow, here oxygen, through the aerosol generation chamber, the CCO particles are fluidized. By a pressure gradient generated by the vacuum pump between the aerosol and the deposition chamber, the particles are accelerated through a convergent 10 mm×0.5 mm slit nozzle. The particles collide with a high velocity (typically above 150 m/s [45]) with the substrate and due to the room temperature impact consolidation (RTIC) mechanism [22,46], a ceramic film forms at room temperature. In case of CCO, a film thickness between 10 μm and 20 μm was achieved. The film thicknesses were measured by a profilometer (waveline 20, Jenoptik AG, Jena, Germany). The morphology, texture, and crystalline phase composition of the CCO films were investigated by scanning electron microscopy (SEM, Zeiss Leo 1530, Oberkochen, Germany) and X-ray diffraction analysis (XRD, Bruker D8 Advance, Billerica, MA, USA).

To evaluate the thermoelectric properties of CCO films, the Seebeck coefficient S and the electrical conductivity σ, were determined. Therefore, the CCO films were deposited on alumina substrates equipped with defined electrode structures (see Fig. 1) and heated in a gas-purgeable furnace from room temperature up to 900 °C.

Here, a constant gas flow of dry synthetic air (20 % O_2 in N_2) was used. A more detailed explanation of the used transducer for simultaneous Seebeck coefficient and resistance measurement can be found in [47,48]. The four-wire resistance R_{4w} was measured by four probe technique with offset compensation (digital multimeter Keithley 2700). The electrical conductivity was calculated according to Eq. (1), wherein s is the spacing between the inner Pt electrodes, R_{4w} is the measured resistance, b the width of the sample, and d the thickness of the CCO film.

$$\sigma_{CCO} = \frac{1}{R_{4w}} \bullet \frac{s}{b \bullet d} \qquad (1)$$
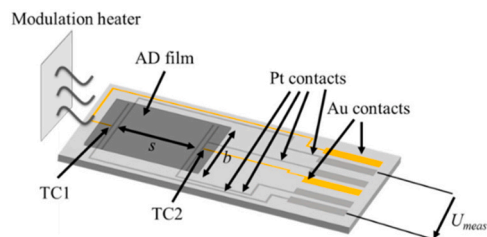

Fig. 1. Seebeck transducer for simultaneous in-plane (*ab*) - Seebeck coefficient determination and 4-wire electrical resistance measurement [47]. Reproduced under terms of the CC-BY license. Copyright 2016 by the authors, published by MDPI, Basel, Switzerland.

$$S_{CCO} = S_{Pt} - \frac{U_{meas}}{\Delta T} \qquad (2)$$

To evaluate the Seebeck coefficient S, the modulation heater in front of the transducer was used to generate an alternating temperature gradient over the transducer and, respectively, over the film. The temperature difference ΔT that occurs over the film (between the thermocouples TC1 and TC2) was determined and the thermovoltage U_{meas} of the CCO film was measured between the Pt contacts of TC1 and TC2. The Seebeck coefficient of the CCO film versus Pt can be determined from U_{meas} by Eq. (2). $U_{meas}/\Delta T$ is evaluated by a regression analysis at each measuring temperature and has to be corrected by the known temperature dependent Seebeck coefficient of platinum S_{Pt}. The measured values required for conductivity and Seebeck were recorded five to seven times in succession for each temperature. From them, the Seebeck coefficient and the conductivity were determined independently of each other. Further details of the evaluation of S can be found in [47,49]. The power factor PF of the CCO films was calculated in dependence on the measuring temperature. To investigate the temperature dependence, the temperature was varied from room temperature to 900 °C in 100 °C steps and the parameters during cooling were also measured. The temperature profile was run twice to characterize the effects of thermal annealing known for PAD films [24,31].

During the measurement, the minimum temperature of the sample was at the specified temperature T and the maximum temperature of the sample was at T + ΔT. For all measurements, ΔT was in the range of 1–2 K. This means that a part of the sample was warmer than specified, but with an error of 1–2 K this deviation is only very small.

3. Results and discussion

The calcined and milled CCO powder has a particle size of $d_{50} = 3.5$ µm. The particle size distribution is shown in Fig. 2a. The as-synthesized CCO powder (Fig. 1b) has a flake-like morphology. The particles show a high aspect ratio (length to height) of about 10, which can be explained by the anisotropic, misfit-layered crystal structure of CCO and the resulting preferred growth directions. In addition, the particles appear frayed, which makes the individual crystal layers of the misfit-layered CCO structure recognizable [10,19,44]. It can be stated that the starting CCO powder for the preparation of thick films by PAD has a texturing with platelet-shaped particles. XRD patterns of the calcined powder can be found in [19].

The crystal structure of the CCO powders and the as-deposited CCO films have been investigated by XRD. Fig. 3 shows the XRD patterns of the CCO reference (a), the calcined CCO powders (b), and of a non-annealed (c) and a thermally annealed (d) CCO PAD film [13]. The comparison between the reference and the CCO powder proves the phase purity [19,44]. No secondary phases or impurities are observed for the powder aerosol deposited CCO film and the positions of the reflexes coincide well.

A phase-pure CCO film was formed by PAD of the platelet-like shaped CCO powder. Two effects are visible comparing the XRD patterns of
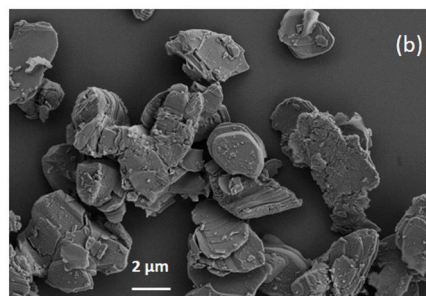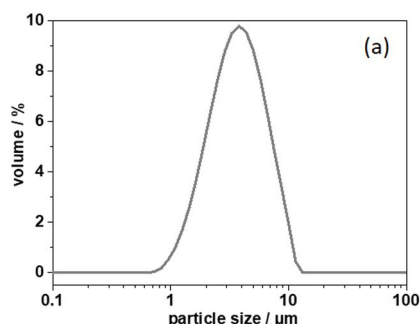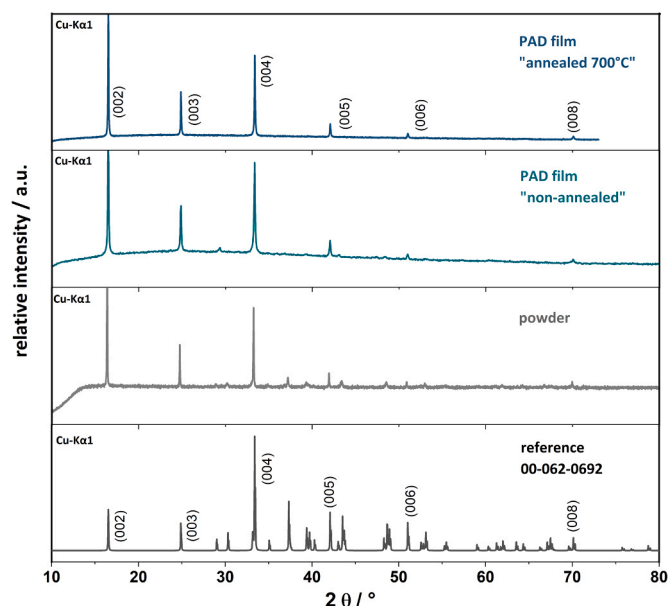
Fig. 3. XRD patterns of different CCO samples: Compared are the reflexes of the reference card (pdf: 00-062-0692) (a) with the synthesized CCO powder (b), a "fresh, non-annealed" PAD film (c) and a thermally at 700°C annealed PAD film (d).

the as-deposited CCO film and the CCO powder. On the one hand, the reflections get broader, which is an indication of either a reduced crystallite size of the films or an introduced microstrain owing to the deposition mechanism or both of these. On the other hand, the XRD-patterns of the as-deposited film shows only (0 0 l) reflections, all other reflections are almost undetectable. This indicates a strong texturing of the PAD CCO film. In accordance to [34,35], the films provide a preferential orientation normal to the substrate plane with a predominant orientation of the grains. The results are also comparable with XRD investigations of pressure-assisted sintered (PAS) CCO tape-casted laminates with a pressure of 7.5 MPa and sintered at 900 °C [19]. Thermal annealing of the PAD CCO films at 700 °C preserves the texturing, but the width of the reflection decreases. This can be attributed to two effects, the relaxation of the microstrain as well as changes in the microstructure like growth of the crystallites [31,34,35]. The XRD results indicate a textured microstructure of the "as-prepared", non-annealed and the "thermal annealed" CCO films with a preferred (0 0 l) orientation. In contrast to [34,35], the as-deposited films also show sharp reflections with a high intensity indicating a comparably high crystallite size and low microstrain. In [34], the aerosol deposited CCO film showed (0 0 l) texture, too. The pole figures in [34] illustrate that the CCO film has a high degree of c-axis orientation. The analysis of the texture by pole figures of the PAD CCO films deposited here to prove the texture is planned for further investigations.

Fig. 2. CCO powder properties: (a) particle size distribution and (b) SEM image of the morphology of as-synthesized CCO powders.

Fig. 4 shows SEM fracture images of the PAD CCO films deposited on alumina substrates. In Fig. 4a, the microstructure of the non-annealed films and a non-typical PAD fracture pattern can be seen. A typical PAD film fracture surface exhibits a fine and grainy structure, uniform particles with very small grains size, and a dense structure [22,23]. The CCO fracture images do not show any distinct fine and grainy stricter indicating nanocrystallinity. Instead, some big crystallites and smaller crystallites can be seen, forming a dense CCO film with no cracks or surface delamination. The films in the thickness range reported in this paper adhere very well, pass the tape test and cannot be scratched off with a scalpel. No delamination is visible in the SEM fracture pattern. Gaps, such as at the interface in Fig. 4a), occur due to pull-out of larger crystals, but are no indication of delamination in this material. Regions where particles appear more deformed rather than fractured and flattened by collision are visible. The flake-like or platelet-like particles are still present. Additionally, regions with fractured particles with smaller sizes are observed. A similar microstructure of an as-deposited CCO film was shown in [34]. According to Furuya et al. [50], two mechanisms for PAD film formation are possible. In the fragmentation mode, the particles fracture and the resulting film microstructure is dominated by fragmented particles with significantly smaller grain sizes than the particle sizes of the powder. Additionally, plastic deformation of the particles can contribute to the formation. The PAD CCO film in Fig. 4a suggests that, both effects contribute to the film formation process. In addition, the orientation and texturing of the film can be seen. As suggested in [50], a plastic deformation of the particles taking place during the deposition could be a hint for film texturing. Additionally, Nakamura et al. discuss that platelet-shaped CCO powder particles preferentially rebreak into a flat and plate-like shape by the PAD deposition mechanism due to the anisotropic layer structure of the CCO crystal. These newly-formed plate-like shaped particles are preferably piled up as a layered structure [35]. Especially for CCO, a misfit-layered material in the form of a flake-like powder is used for the deposition process and the resulting as-deposited films provide preferred orientation of the CCO grains.

The thermally annealed CCO films (3 h at 900 °C) appear in a stacked lamellar structure with platelet-shaped CCO particles, clearly visible in Fig. 4b. The film consists of grains oriented with their *c*-axis orthogonal to the substrate surface. Compared to the as-deposited films, the grains have grown along the *ab*-direction parallel to the substrate surface. A textured microstructure and the individual crystal layers of the CCO structure are visible. The morphology of the films after the thermal treatment shows strongly aligned crystallites resulting in a strong texture of the films. Due to the thermal annealing at 900 °C, different processes occur. Grain growth of the CCO grains takes place and the crystallization is enhanced. In addition, structural defects are minimized and the microstrain is getting relaxed. Which of the processes dominates at which temperature has not been clarified yet. These processes led to the morphological changes visible in Fig. 4b and affect the thermoelectric properties of the CCO film. The influence of the PAD CCO film morphology and the morphological changes during thermal annealing on the thermoelectric properties in *ab*-direction (in-plane of the film) will be described and discussed in the following part.
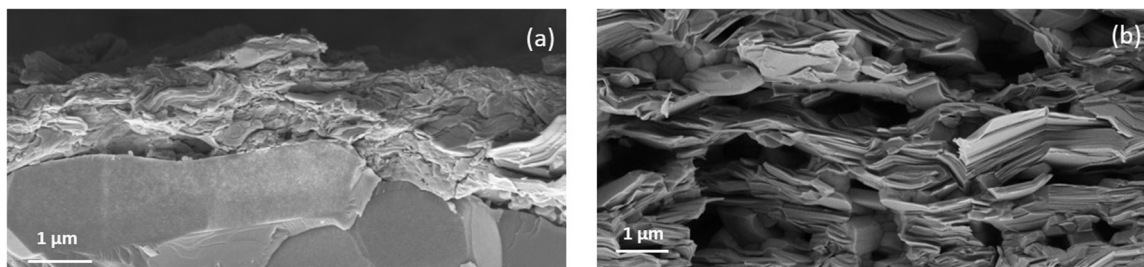
The behavior of the Seebeck coefficient *S*, investigated in *ab*-direction of the CCO PAD film, is plotted in Fig. 5 in dependence on the measuring temperature in dry synthetic air. First, it should be mentioned that the first value of the Seebeck coefficient was measured at room temperature with a fresh, as-deposited PAD CCO film without any thermal treatment. Additionally, in Fig. 5, the Seebeck coefficients of tape-casted and pressure-assisted sintered (PAS) CCO laminates from the same powder as bulk materials with different porosities (50 %, 25 %, and 6 %) are shown for comparison (data from [19]). As a first result, the Seebeck coefficient of the CCO PAD film during the first heating cycle (CCO PAD 1st) from room temperature to 900 °C is very close to that of the PAS CCO laminates [19]. *S* is around 100 μV/K at room temperatures and reaches values around 170 μV/K at 900 °C. The behavior of the CCO PAD film is similar to the sintered laminates and shows the same temperature dependence. The Seebeck coefficient reaches the values measured of Co349 single crystals [13] and shows comparable values to [34,35].

After 900 °C, the sample was cooled down to room temperature and the 2nd heating cycle (CCO PAD 2nd) started. Comparing the *S* value at room temperature before and after thermal treatment at 900 °C, no huge differences can be found. *S* at room temperature is still between 90 and 120 μV/K. This means, the value of the Seebeck coefficient is neither affected by the thermal treatment nor by the previously discussed morphological changes of the CCO PAD film. This behavior was expected, since the Seebeck coefficient is almost independent on geometry, porosity, and morphological changes [51–53]. The second heating cycle up to 800 °C provides comparable Seebeck coefficients. However, at 900 °C and during the 2nd cooling cycle, significantly higher Seebeck coefficients (up to 225 μV/K) could be measured. This strong increase in
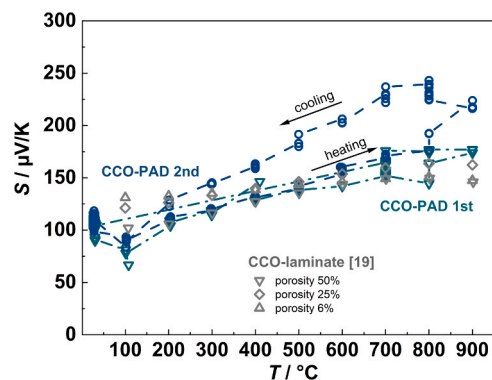
Fig. 5. In-plane (*ab*) Seebeck coefficient *S* of a CCO PAD film in dependence on temperature for two heating and cooling cycles (1st and 2nd). All independently determined data points are entered for each temperature. Some of these are also superimposed. For all data points, however, the scatter is below the 10 % frequently mentioned for determining the Seebeck coefficient. For comparison, *S* of tape-casted and pressure assisted sintered CCO laminates from the same powder (CCO laminate) with different porosities (50 %, 25 % and 6 %, depending on the pressure during sintering, the porosity was determined by Archimedes method) are shown [19].

Fig. 4. SEM fracture images: (a) as-prepared CCO PAD-film on an alumina substrate (non-annealed); (b) CCO PAD film after 900 °C thermal annealing.

Seebeck coefficient cannot be explained, yet. In [54,55], it is discussed that the oxygen partial pressure at elevated temperatures and during annealing at high temperatures has an influence on the oxygen vacancy concentration. As a consequence, the charge carrier density may have changed. This would affect the Seebeck coefficient and also the electrical conductivity. Further investigations on the influence of, e.g., doping of the CCO film by diffusion processes, the oxygen concentration and the thermal post-treatment time are necessary.

The second relevant physical property for thermoelectric materials is the electrical conductivity σ of the CCO film in *ab*-direction (Fig. 6). To classify the results of the PAD CCO film, the electrical conductivities determined on PAS CCO laminates of different porosity (depending on the pressure during sintering) are added data from [19]. The electrical conductivity of the PAS CCO laminates shows a clear dependence on the porosity of the laminates, however σ is almost independent on the measuring temperature. The highest electrical conductivity (around 150 S/cm) could be determined for a PAS CCO laminate with lowest porosity of 6 %. The CCO PAD film shows the typical behavior of a PAD film in terms of electrical conductivity. At room temperature, the electrical conductivity of the fresh, as-deposited CCO PAD films is low. However, it increases significantly with measuring temperature. The measuring temperature is in this case equivalent to the thermal annealing temperature (the holding time of each temperature step is approx. 3 h). Up to 300 °C, a clear increase in electrical conductivity can be seen. At 300 °C, the electrical conductivity of the PAD CCO film reaches the value of the CCO laminate with 6 % porosity of around 150 S/cm. Up to 500 °C, σ remains then almost constant with a slight drop. Further heating up to 900 °C results in another significant conductivity increase and σ reaches values of 275 S/cm at 900 °C. The strong increase in σ of the CCO PAD film may be explained by two effects. First, during thermal treatment, the induced microstrain in the PAD film relaxes, which results in an increasing electrical conductivity, as it is often seen for PAD films [24,31]. Second, as previously explained, the morphology changes during thermal treatment and a higher electrical conductivity occurs due to the oriented crystal growth in-plane (*ab*) direction. Compared to PAS CCO laminate reference values, the thermally annealed (900 °C) CCO PAD film provides a significantly higher in-plane electrical conductivity. At the same time, the determined electrical conductivity is significantly increased compared to that of other aerosol deposited CCO films [34,35]. The higher electrical conductivity can be explained on the one hand by a very low porosity within the CCO PAD film (almost dense films, as shown in Fig. 4b) and on the other hand by the strongly oriented crystallite growth in-plane direction (see Fig. 4b) and the occurring crystallization during thermal
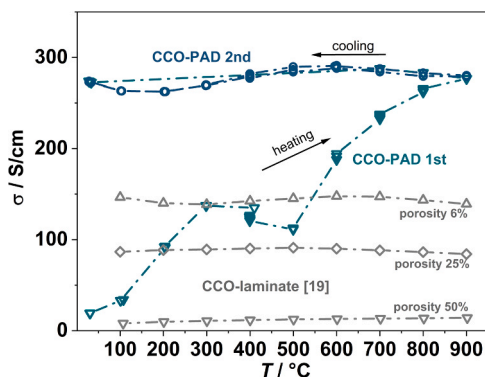
annealing especially at 900 °C [34]. After annealing at 900 °C (after the 1st heating cycle), the electrical conductivity remains almost constant at around 275 S/cm and is almost independent on the measuring temperature. Also, in the 2nd heating and cooling cycle, the electrical conductivity remains almost constant and shows only a slight dependence on the temperature. These stable electrical conductivity values indicate that the processes of microstrain relaxation and thermally induced crystallite growth are almost completed after the first annealing step at 900 °C [24,29,31,56]. The shown results with an optimal thermal annealing temperature at 900 °C for highest thermoelectric properties are in good agreement with [34,35]. It should be noted that 1st thermal treatment of the CCO PAD films at 900 °C is necessary to obtain the maximum electrical in-plane conductivity, while the effects of the 1st annealing on the Seebeck coefficient are negligible.

The power factor *PF* of the PAD CCO films, as derived from the data in Fig. 5 and Fig. 6, illustrates the good thermoelectric properties of the thermally annealed PAD films compared to a PAS CCO laminate with 6 % porosity (Fig. 7). The PAS CCO laminate has a *PF* between 270 and 300 μW/mK^2 and is almost independent on temperature. The "fresh" CCO PAD film, directly after deposition, shows during the 1st heating cycle a lower *PF* from room temperature to approx. 500 °C due to the lower electrical conductivity of the non-annealed PAD films. As the temperature increases, which in the 1st heating cycle corresponds to the annealing temperature, the *PF* increases significantly and reaches at 900 °C values around 850 μW/mK^2 (this is an increase of three times compared to the PAS CCO laminate). This strong improvement is due to the huge increase in electrical conductivity of the PAD film during the 1st heating cycle at high temperatures and the occurring thermal annealing processes. After cooling down, the *PF* at room temperature of the PAD CCO film is between 300 and 350 μW/mK^2.

During the 2nd heating cycle, the *PF* increases and up to 800 °C, the *PF* values at 700 °C and 800 °C are comparable to the 1st cooling cycle. Due to the occurring increase in *S* during the 2nd heating cycle above 800 °C and during the 2nd cooling cycle, the *PF* increases significantly, too. At 600 °C, in the 2nd cooling cycle, the *PF* reaches a value of 1225 μV/mK^2 and has a maximum value at 800 °C and 900 ° around 1500 μV/mK^2. Compared to literature at 600 °C, the single crystal provides a *PF* of 3000 μV/mK^2 [10] and the PAS CCO laminate (6 % porosity, 7.5 MPa) has a *PF* of 320 μV/mK^2 [19]. The PAD CCO film thus reaches approx. 40 % of the *PF* of the single crystal value (2nd cooling cycle) and 25 % during the 1st cooling cycle (each at 600 °C). Compared to CCO bulk literature and to literature of PAD films [34,35], the PAD CCO films of this work provide the highest *PF* values for polycrystalline CCO. To highlight this, Fig. 8 compares the in-plane (*ab*) thermoelectric properties of variously synthesized CCO materials (single crystal, bulk, laminates, PAD films) in the Ioffe diagram at 600 °C [14,17–20,34,35,
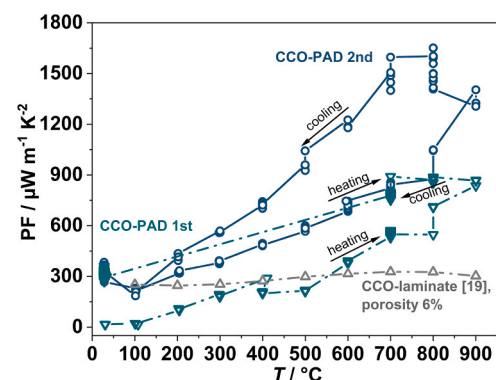

Fig. 6. In-plane (*ab*) electrical conductivity σ of a CCO PAD film in dependence on temperature for two heating and cooling cycles (1st and 2nd). All independently determined data points are entered for each temperature. Some of these are also superimposed. For comparison, σ of tape-casted and pressure assisted sintered CCO laminates from the same powder (CCO laminate) with different porosities (50 %, 25 % and 6 %, depending on the pressure during sintering, the porosity was determined by Archimedes method) are shown [19].

Fig. 7. In-plane (*ab*) Power Factor *PF* of a CCO PAD film in dependence on temperature for two heating and cooling cycles (1st and 2nd). All independently determined data points are entered for each temperature. Some of these are also superimposed. The *PF* of tape-casted PAS CCO laminates from the same powder (CCO-laminate, 6 % porosity) are shown [19].
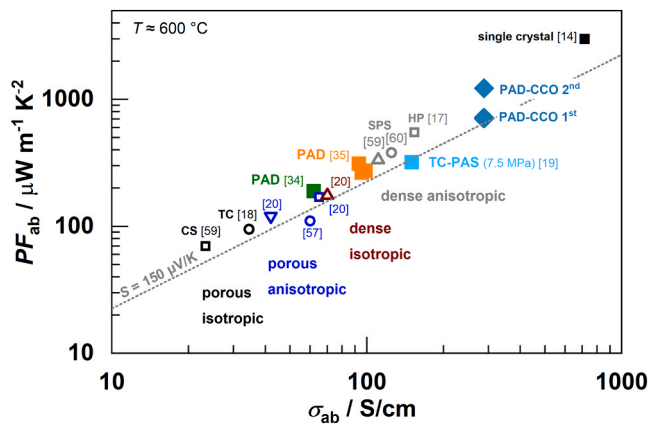
Fig. 8. Power factor *PF* and electrical conductivity σ at 600 °C in-plane (*ab*) of the PAD CCO film in Ioffe representation compared with literature data [14, 17–20,34,35,57,59,60].

57–60]. In addition to conventional (CS), pressure-assisted (PAS) and spark plasma (SPS) sintering, hot pressing (HP) is used as a manufacturing method. To support the texturing of the CCO, tape casting (TC) is a possible method in combination with the various sintering processes. Additionally, the results of PAD films (PAD) are shown. The results of the PAD CCO films of this work fit very well into the trend of the literature data. Depending on the processing method of the CCO, different microstructures, porosities, and textures result for the CCO samples. These parameters directly affect the thermoelectric parameters in the Ioffe diagram, i.e., the power factor PF_{ab} caused by variations in the electrical conductivity σ_{ab}. The Seebeck coefficient S_{ab} of the different samples is almost constant in the range of 150 µV/K at 600 °C, while the electrical conductivity in-plane (σ_{ab}) shows a clear dependence on the manufacturing process and thus on the microstructure. As discussed in [61], the microstructure of CCO samples can be classified in four regions, which are shown in Fig. 8 in different colors: porous isotropic, porous anisotropic, dense isotropic and dense anisotropic. An increase in the density of the CCO sample (lower porosity) and an increase in the anisotropy in the *ab*-direction (in-plane) strongly influence the conductivity of the sample σ_{ab}, which eventually leads to an increase in *PF* and, hence, the thermoelectric properties are closer to the values of the single crystal. For the PAD CCO films, it can be deduced from the results that they have a high density (low porosity) and a strong texture compared to other CCO samples and PAD films. The PAD CCO films are almost dense and the anisotropy and texture of the films, especially after thermal annealing at 900 °C, have been shown in the REM and XRD investigations. The dense and anisotropic films therefore provide the highest *PF* and electrical conductivity. In a next step, the *MRD* for the PAD CCO films will be investigated.

4. Conclusions

The discussed morphological investigations and the determined thermoelectric parameters *S*, σ_{ab}, and *PF* show that the PAD CCO films have very good in-plane (*ab*-direction) thermoelectric characteristics. After thermal annealing of the PAD CCO films, the largest value for *PF* compared to the literature is observed. The values reach about 40 % of the *PF* value of the single crystal, which is much higher than comparable CCO bulks or CCO laminates reported in literature. By thermally annealing of CCO PAD film (once at 900 °C), the electrical conductivity increases very significantly and reaches values higher than those of conventionally prepared CCO bulk ceramics. The film has an electrical conductivity of 19.3 S/cm in the as-deposited state. During thermal annealing, the conductivity increases to 279 S/cm at 900 °C. After cooling, the electrical conductivity of the now heat-treated film is 273 S/cm In contrast, the Seebeck coefficient remains almost unaffected by the

annealing temperature and is comparable to that of CCO laminates. It increases from approx. 90 µV/K at room temperature to approx. 180 µm/K at 900 °C. The 2nd thermal annealing cycle does not change the electrical conductivity anymore, it remains in the range between 260 S/cm and 295 S/cm, but it leads to an increase of the Seebeck coefficient up to approximately 240 µV/K at 800 °C. This needs to be investigated in more detail in future work, as well as the effect of significantly more than two heating and cooling cycles. The long-term influence of high temperature should also be investigated. The excellent thermoelectric properties of the PAD CCO film after thermal annealing may be explained as follows. First, a dense CCO film is produced by PAD, which shows an oriented and textured morphology in the preferred *ab*-direction. Second, the thermal treatment relaxes the microstrain, that hinders the electrical conductivity (at less than 500 °C), and at 900 °C crystal growth in preferential *ab*-direction occurs.

Future work needs to clarify, which of the occurring processes is responsible for the change in thermoelectric properties and morphology. The relationship between the thermoelectric properties and the film morphology as a function of the thermal annealing parameters will be further investigated. The analysis of the texture of the PAD CCO films by pole figures is necessary to determine the *MRD* value. For *ZT*, the thermal conductivity of the films has to be investigated. Due to the anisotropy of the CCO PAD films, the thermoelectric parameters in-plane and through-plane are necessary. DSC measurements should be carried out to detect crystallization effects. Changes in the oxygen vacancy concentration could be determined using (high temperature) XRD, possibly also on the powder. In addition, the measurements could be repeated under different oxygen partial pressures.

CRediT authorship contribution statement

Sophie Bresch: Writing – review & editing, Writing – original draft, Resources. **Ralf Moos:** Writing – review & editing, Supervision, Conceptualization. **Daniela Schönauer-Kamin:** Writing – review & editing, Writing – original draft, Supervision, Investigation, Conceptualization. **Daniel Paulus:** Writing – review & editing, Writing – original draft, Investigation.

Declaration of Competing Interest

The authors declare that they have no known competing financial interests or personal relationships that could have appeared to influence the work reported in this paper.

Acknowledgments

Appendix A. Supporting information

Supplementary data associated with this article can be found in the online version at doi:10.1016/j.jeurceramsoc.2024.116717.

References

[1] H. Jouhara, A. Żabnieńska-Góra, N. Khordehgah, Q. Doraghi, L. Ahmad, L. Norman, B. Axcell, L. Wrobel, S. Dai, Thermoelectric generator (TEG) technologies and applications, Int. J. Thermofluids 9 (2021) 100063, https://doi.org/10.1016/j.ijft.2021.100063.

[2] A. Montecucco, J. Siviter, A.R. Knox, The effect of temperature mismatch on thermoelectric generators electrically connected in series and parallel, Appl. Energy 123 (2014) 47–54, https://doi.org/10.1016/j.apenergy.2014.02.030.

[3] J. Martin, Apparatus for the high temperature measurement of the Seebeck coefficient in thermoelectric materials, Rev. Sci. Instrum. 83 (2012) 65101, https://doi.org/10.1063/1.4723872.

[4] G.J. Snyder, A.H. Snyder, Figure of merit ZT of a thermoelectric device defined from materials properties, Energy Environ. Sci. 10 (2017) 2280–2283, https://doi.org/10.1039/C7EE02007D.

[5] G. Snyder, Thermoelectric Power Generation: Efficiency and Compatibility, in: Thermoelectrics Handbook, pp. 9–19.

[6] C.B. Vining, An inconvenient truth about thermoelectrics, Nat. Mater. 8 (2009) 83–85, https://doi.org/10.1038/nmat2361.

[7] M. Wolf, R. Hinterding, A. Feldhoff, High power factor vs. high zT—a review of thermoelectric materials for high-temperature application, Entropy 21 (2019) 1058, https://doi.org/10.3390/e21111058.

[8] D. Narducci, Do we really need high thermoelectric figures of merit? A critical appraisal to the power conversion efficiency of thermoelectric materials, Appl. Phys. Lett. 99 (2011) 102104, https://doi.org/10.1063/1.3634018.

[9] I.T. Witting, T.C. Chasapis, F. Ricci, M. Peters, N.A. Heinz, G. Hautier, G.J. Snyder, The thermoelectric properties of Bismuth Telluride, Adv. Elect. Mater. 5 (2019) 1800904, https://doi.org/10.1002/aelm.201800904.

[10] K. Koumoto, R. Funahashi, E. Guilmeau, Y. Miyazaki, A. Weidenkaff, Y. Wang, C. Wan, Thermoelectric ceramics for energy harvesting, J. Am. Ceram. Soc. 96 (2013) 1–23, https://doi.org/10.1111/jace.12076.

[11] J.W. Fergus, Oxide materials for high temperature thermoelectric energy conversion, J. Eur. Ceram. Soc. 32 (2012) 525–540, https://doi.org/10.1016/j.jeurceramsoc.2011.10.007.

[12] R. Funahashi, T. Barbier, E. Combe, Thermoelectric materials for middle and high temperature ranges, J. Mater. Res. 30 (2015) 2544–2557, https://doi.org/10.1557/jmr.2015.145.

[13] A.C. Masset, C. Michel, A. Maignan, M. Hervieu, O. Toulemonde, F. Studer, B. Raveau, J. Hejtmanek, Misfit-layered cobaltite with an anisotropic giant magnetoresistance: Ca$_3$Co$_4$O$_9$, Phys. Rev. B 62 (2000) 166–175, https://doi.org/10.1103/PhysRevB.62.166.

[14] R. Funahashi, I. Matsubara, H. Ikuta, T. Takeuchi, U. Mizutani, S. Sodeoka, An oxide single crystal with high thermoelectric performance in air, Jpn. J. Appl. Phys. 39 (2000) L1127, https://doi.org/10.1143/JJAP.39.L1127.

[15] D. Kenfaui, B. Lenoir, D. Chateigner, B. Ouladdiaf, M. Gomina, J.G. Noudem, Development of multilayer textured Ca$_3$Co$_4$O$_9$ materials for thermoelectric generators: Influence of the anisotropy on the transport properties, J. Eur. Ceram. Soc. 32 (2012) 2405–2414, https://doi.org/10.1016/j.jeurceramsoc.2012.03.022.

[16] E. Woermann, A. Muan, Phase equilibria in the system CaO-cobalt oxide in air, J. Inorg. Nucl. Chem. 32 (1970) 1455–1459, https://doi.org/10.1016/0022-1902(70)80631-5.

[17] D. Kenfaui, D. Chateigner, M. Gomina, J.G. Noudem, Anisotropy of the mechanical and thermoelectric properties of hot-pressed single-layer and multilayer thick Ca$_3$Co$_4$O$_9$ ceramics, Int. J. Appl. Ceram. Technol. 8 (2011) 214–226, https://doi.org/10.1111/j.1744-7402.2009.02431.x.

[18] I.V. Matsukevich, A.I. Klyndyuk, E.A. Tugova, A.N. Kovalenko, A.A. Marova, N. S. Krasutskaya, Thermoelectric properties of Ca$_{3-x}$ Bi$_x$ Co$_4$O$_{9+\delta}$ (0.0 ⩽ x ⩽ 1.5) ceramics, Inorg. Mater. 52 (2016) 593–599, https://doi.org/10.1134/S0020168516060091.

[19] S. Bresch, B. Mieller, D. Schönauer-Kamin, R. Moos, T. Reimann, F. Giovannelli, T. Rabe, Influence of pressure and dwell time on pressure-assisted sintering of calcium cobaltite, J. Am. Ceram. Soc. 104 (2021) 917–927, https://doi.org/10.1111/jace.17541.

[20] T. Schulz, T. Reimann, A. Bochmann, A. Vogel, B. Capraro, B. Mieller, S. Teichert, J. Töpfer, Sintering behavior, microstructure and thermoelectric properties of calcium cobaltite thick films for transversal thermoelectric multilayer generators, J. Eur. Ceram. Soc. 38 (2018) 1600–1607, https://doi.org/10.1016/j.jeurceramsoc.2017.11.017.

[21] J. Akedo, Aerosol deposition method for fabrication of nano crystal ceramic layer, MSF 449-452 (2004) 43–48, https://doi.org/10.4028/www.scientific.net/MSF.449-452.43.

[22] J. Akedo, Room temperature impact consolidation (RTIC) of fine ceramic powder by aerosol deposition method and applications to microdevices, J. Therm. Spray. Tech. 17 (2008) 181–198, https://doi.org/10.1007/s11666-008-9163-7.

[23] M. Schubert, D. Hanft, T. Nazarenus, J. Exner, M. Schubert, P. Nieke, P. Glosse, N. Leupold, J. Kita, R. Moos, Powder aerosol deposition method — novel applications in the field of sensing and energy technology, Funct. Mater. Lett. 12 (2019) 1930005, https://doi.org/10.1142/S1793604719300056.

[24] T. Nazarenus, K. Schlesier, F. Lebeda, M. Retsch, R. Moos, Microstrain release decouples electronic and thermal conductivity in powder aerosol deposited films, Mater. Lett. 322 (2022) 132461, https://doi.org/10.1016/j.matlet.2022.132461.

[25] M. Sozak, T. Nazarenus, J. Exner, J. Kita, R. Moos, Room temperature manufacture of dense NaSICON solid electrolyte films for all-solid-state-sodium batteries, J. Mater. Sci. 58 (2023) 10108–10119, https://doi.org/10.1007/s10853-023-08642-w.

[26] J. Akedo, Room temperature impact consolidation and application to ceramic coatings: aerosol deposition method, J. Ceram. Soc. Jpn. 128 (2020) 101–116, https://doi.org/10.2109/jcersj2.19196.

[27] S. Baba, L. Huang, H. Sato, R. Funahashi, J. Akedo, Room-temperature fast deposition and characterization of nanocrystalline Bi$_{0.4}$Sb$_{1.6}$Te$_3$ thick films by aerosol deposition, J. Phys.: Conf. Ser. 379 (2012) 12011, https://doi.org/10.1088/1742-6596/379/1/012011.

[28] R. Werner, J.S. Matejka, D. Schönauer-Kamin, R. Moos, From thermoelectric powder directly to thermoelectric generators: flexible Bi$_2$Te$_3$ films on polymer sheets prepared by the powder aerosol deposition method at room temperature, Energy Tech. 10 (2022) 2101091, https://doi.org/10.1002/ente.202101091.

[29] T. Nazarenus, K. Schlesier, S. Biberger, J. Exner, J. Kita, A. Köhler, R. Moos, Posttreatment of powder aerosol deposited oxide ceramic films by high power LED, Int. J. Appl. Ceram. Technol. 19 (2022) 1540–1553, https://doi.org/10.1111/ijac.13977.

[30] D. Paulus, J. Kita, R. Moos, Relaxation behavior of intrinsic compressive stress in powder aerosol co-deposited films: rethinking PAD films as nanomaterials, Ceram. Int. 49 (2023) 38375–38381, https://doi.org/10.1016/j.ceramint.2023.09.065.

[31] J. Exner, T. Nazarenus, D. Hanft, J. Kita, R. Moos, What happens during thermal post-treatment of powder aerosol deposited functional ceramic films? Explanations based on an experiment-enhanced literature survey, Adv. Mater. 32 (2020) e1908104, https://doi.org/10.1002/adma.201908104.

[32] F. Zhuo, U. Eckstein, N.H. Khansur, C. Dietz, D. Urushihara, T. Asaka, K. Kakimoto, K.G. Webber, X. Fang, J. Rödel, Temperature-induced changes of the electrical and mechanical properties of aerosol-deposited BaTiO$_3$ thick films for energy storage applications, J. Am. Ceram. Soc. 105 (2022) 4108–4121, https://doi.org/10.1111/jace.18377.

[33] J.J. Choi, J.H. Jang, D.S. Park, B.D. Hahn, W.H. Yoon, C. Park, Electrical properties of lead zinc niobate - lead zirconate titanate thick films formed by aerosol deposition process, Solid State Phenom. 124-126 (2007) 169–172, https://doi.org/10.4028/www.scientific.net/SSP.124-126.169.

[34] W.-H. Yoon, J. Ryu, J.-J. Choi, B.-D. Hahn, J.H. Choi, B.-K. Lee, J.-H. Cho, D.-S. Park, Enhanced thermoelectric properties of textured Ca$_3$Co$_4$O$_9$ thick film by aerosol deposition, J. Am. Ceram. Soc. 93 (2010) 2125–2127, https://doi.org/10.1111/j.1551-2916.2010.03674.x.

[35] Y. Nakamura, Y. Matsufuji, M. Inoue, Fabrication and properties of thermoelectric oxide thick films deposited with aerosol deposition method, J. Phys.: Conf. Ser. 352 (2012) 12026, https://doi.org/10.1088/1742-6596/352/1/012026.

[36] T. Reimann, A. Bochmann, A. Vogel, B. Capraro, S. Teichert, J. Töpfer, Fabrication of a transversal multilayer thermoelectric generator with substituted calcium manganite, J. Am. Ceram. Soc. 100 (2017) 5700–5708, https://doi.org/10.1111/jace.15119.

[37] A. Bochmann, T. Reimann, T. Schulz, S. Teichert, J. Töpfer, Transverse thermoelectric multilayer generator with bismuth-substituted calcium cobaltite: design optimization through variation of tilt angle, J. Eur. Ceram. Soc. 39 (2019) 2923–2929, https://doi.org/10.1016/j.jeurceramsoc.2019.03.036.

[38] J. Töpfer, T. Reimann, T. Schulz, A. Bochmann, B. Capraro, S. Barth, A. Vogel, S. Teichert, Oxide multilayer thermoelectric generators, Int. J. Appl. Ceram. Technol. 15 (2018) 716–722, https://doi.org/10.1111/ijac.12822.

[39] S. Bresch, B. Mieller, P. Mrkwitschka, R. Moos, T. Rabe, Glass-ceramic composites as insulation material for thermoelectric oxide multilayer generators, J. Am. Ceram. Soc. 105 (2022) 2140–2149, https://doi.org/10.1111/jace.18235.

[40] R.A. Dorey, Integrated powder-based thick films for thermoelectric, pyroelectric, and piezoelectric energy harvesting devices, IEEE Sens. J. 14 (2014) 2177–2184, https://doi.org/10.1109/JSEN.2014.2306443.

[41] A.R.M. Siddique, S. Mahmud, B. van Heyst, A review of the state of the science on wearable thermoelectric power generators (TEGs) and their existing challenges, Renew. Sustain. Energy Rev. 73 (2017) 730–744, https://doi.org/10.1016/j.rser.2017.01.177.

[42] J. Yu, R. Freer, Calcium cobaltite, a promising oxide for energy harvesting: effective strategies toward enhanced thermoelectric performance, J. Phys. Energy 4 (2022) 22001, https://doi.org/10.1088/2515-7655/ac5172.

[43] K.V. Selvan, M.N. Hasan, M.S. Mohamed Ali, Methodological reviews and analyses on the emerging research trends and progresses of thermoelectric generators, Int. J. Energy Res 43 (2019) 113–140, https://doi.org/10.1002/er.4206.

[44] S. Bresch, B. Mieller, D. Schoenauer-Kamin, R. Moos, F. Giovanelli, T. Rabe, Influence of pressure assisted sintering and reaction sintering on microstructure and thermoelectric properties of bi-doped and undoped calcium cobaltite, J. Appl. Phys. 126 (2019) 075102, https://doi.org/10.1063/1.5107476.

[45] H. Katanoda, K. Matsuo, Gasdynamic simulation of aerosol deposition method, Mater. Trans. 47 (2006) 1620–1625, https://doi.org/10.2320/matertrans.47.1620.

[46] J. Akedo, S. Nakano, J. Park, S. Baba, K. Ashida, The aerosol deposition method, Synth. Engl. Ed. 1 (2008) 121–130, https://doi.org/10.5571/syntheng.1.121.

[47] T. Stöcker, J. Exner, M. Schubert, M. Streibl, R. Moos, Influence of oxygen partial pressure during processing on the thermoelectric properties of aerosol-deposited CuFeO$_2$, Materials 9 (2016) https://doi.org/10.3390/ma9040227.

[48] M. Bektas, T. Stöcker, A. Mergner, G. Hagen, R. Moos, Combined resistive and thermoelectric oxygen sensor with almost temperature-independent characteristics, J. Sens. Sens. Syst. 7 (2018) 289–297, https://doi.org/10.5194/jsss-7-289-2018.

[49] F. Rettig, R. Moos, Direct thermoelectric gas sensors: design aspects and first gas sensors, Sens. Actuators B: Chem. 123 (2007) 413–419, https://doi.org/10.1016/j.snb.2006.09.002.

[50] Y. Furuya, S. Konuma, M. Hasegawa, Deposition mechanism of alumina particles in aerosol deposition based on the kinetic energy of particles, Surf. Coat. Technol. 458 (2023) 129362, https://doi.org/10.1016/j.surfcoat.2023.129362.

[51] J. Martin, T. Tritt, C. Uher, High temperature Seebeck coefficient metrology, J. Appl. Phys. 108 (2010) 121101, https://doi.org/10.1063/1.3503505.

[52] P. Gerthsen, K.H. Härdtl, A. Csillag, Mobility determinations from weight measurements in solid solutions of (Ba, Sr) TiO$_3$, Phys. Stat. Sol. (a) 13 (1972) 127–133, https://doi.org/10.1002/pssa.2210130113.

[53] G.J. Snyder, A. Pereyra, R. Gurunathan, Effective mass from seebeck coefficient, Adv. Funct. Mater. 32 (2022) 2112772, https://doi.org/10.1002/adfm.202112772.

[54] D. Moser, L. Karvonen, S. Populoh, M. Trottmann, A. Weidenkaff, Influence of the oxygen content on thermoelectric properties of $Ca_{3-x}Bi_xCo_4O_{9+\delta}$ system, Solid State Sci. 13 (2011) 2160–2164, https://doi.org/10.1016/j. solidstatesciences.2011.10.001.

[55] J. Shimoyama, S. Horii, K. Otzschi, M. Sano, K. Kishio, Oxygen nonstoichiometry in layered cobaltite $Ca_3Co_4O_y$, Jpn. J. Appl. Phys. 42 (2003) L194–L197, https://doi. org/10.1143/JJAP.42.L194.

[56] T. Nazarenus, J. Schneider, L. Hennerici, R. Moos, J. Kita, Energy estimation of the post-treatment process for powder aerosol deposited solid electrolyte films, Funct. Mater. Lett. 16 (2023) 2350014, https://doi.org/10.1142/S1793604723500145.

[57] H. Su, Y. Jiang, X. Lan, X. Liu, H. Zhong, D. Yu, $Ca_{3-x}Bi_xCo_4O_9$ and $Ca_{1-y}Sm_yMnO_3$ thermoelectric materials and their power-generation devices, Phys. Stat. Sol. (a) 208 (2011) 147–155, https://doi.org/10.1002/ pssa.201026347.

[58] D. Kenfaui, G. Bonnefont, D. Chateigner, G. Fantozzi, M. Gomina, J.G. Noudem, $Ca_3Co_4O_9$ ceramics consolidated by SPS process: optimisation of mechanical and thermoelectric properties, Mater. Res. Bull. 45 (2010) 1240–1249, https://doi.org/ 10.1016/j.materresbull.2010.05.006.

[59] D. Kenfaui, D. Chateigner, M. Gomina, J.G. Noudem, Texture, mechanical and thermoelectric properties of $Ca_3Co_4O_9$ ceramics, J. Alloy. Compd. 490 (2010) 472–479, https://doi.org/10.1016/j.jallcom.2009.10.048.

[60] Z. Shi, T. Su, P. Zhang, Z. Lou, M. Qin, T. Gao, J. Xu, J. Zhu, F. Gao, Enhanced thermoelectric performance of $Ca_3Co_4O_9$ ceramics through grain orientation and interface modulation, J. Mater. Chem. A 8 (2020) 19561–19572, https://doi.org/ 10.1039/D0TA07007F.

[61] S. Bresch. Oxidkeramische Werkstoffe und Folien für thermoelektrische Multilayergeneratoren, Bayreuther Beiträge zu Materialien und Prozessen, PhD-Thesis, first, ed., Shaker, Düren, 2022 https://doi.org/10.2370/9783844088021.